Tunability of RF-Responses by Plasmonic Dielectric Amplification Using Branched e−-Polarizable C$_{60}$-Adducts on Magnetic Nanoparticles

Min Wang,[†] Tzuyang Yu,[‡] Loon-Seng Tan,[§] Augustine Urbas,[§] and Long Y. Chiang[*,†]

[†]Department of Chemistry, University of Massachusetts—Lowell, Lowell, Massachusetts 01854, United States
[‡]Department of Civil and Environmental Engineering, University of Massachusetts—Lowell, Lowell, Massachusetts 01854, United States
[§]Functional Materials Division, AFRL/RXA, Air Force Research Laboratory, Wright-Patterson Air Force Base, Dayton, Ohio 45433, United States

S *Supporting Information*

ABSTRACT: Three C$_{60}$-DPAF conjugates were synthesized with one as a linear monoadduct and two as branched or starburst multiadducts in structure for the investigation of chromophore antenna number-dependent tunability of RF-responses at 0.5−18 GHz. The effect was photoinduced by the generation of surface plasmonic resonance (SPR) at the surface of trilayered core−shell nanoparticles (NPs) consisting of a highly magnetic γ-FeO$_x$@AuNP core and an e−-polarizable C$_{60}$-DPAF adduct-derived partially bilayered fullerosome outer shell. Observed large dielectric (permittivity) amplification phenomena, with the maximization on the starburst multiadduct-derived nanoparticles, were correlated to the photoactivation efficiency at the gold nanolayer. We hypothesized

(γ-FeO$_x$@AuNP)@[C$_{60}$(>DPAF-C$_9$)$_x$]$_n$

that the prolong accumulation (or trapping) of photogenerated SPR energy in the intermediate gold layer, sandwiched between the C$_{60}$(>DPAF-C$_9$)$_x$-derived fullerosome membrane and the highly magnetic γ-FeO$_x$ NP core, was effectively released at the light-off stage to induce the intramolecular polarization of C$_{60}$-DPAF adducts. Resulting charged transient states were regarded as the origin of observed high permittivity-photoswitching effect. Similar tunability capabilities in subsequent measurements of distant monostatic and angle-dependent bistatic reflective SAR images might provide insights to RF-signal modulation in coating applications and the potential use of these nanomaterials as permittivity-photoswitching agents in RF-frequency devices.
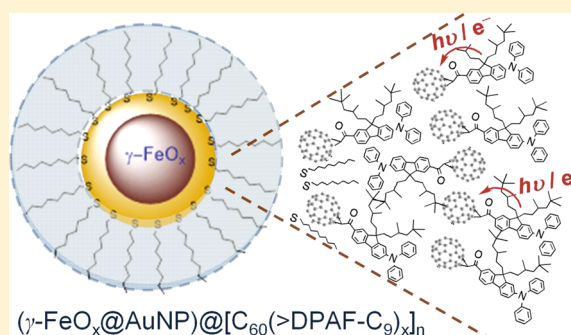
1. INTRODUCTION

Plasmonic metallic nanoparticles[1,2] (NPs) capable of producing photoinduced surface plasmon resonance (SPR) energy can lead to the formation of polarizations at the surface region. Polarizability of this particular type of NPs, as a function of the size, refractive index, shape, density, and surrounding medium, is the factor to influence the state of scattering and absorption of light, e.g., absorption cross-section enhancement, as demonstrated in several theoretical studies.[3,4] The phenomena of light-trapping effect in a thin-film structure can be achieved by implanting or embedding SPR-producing metallic NPs in a medium of dielectric materials.[4] It involves a process that is possible to concentrate or fold the incident photon energy in terms of plasmon oscillations. In such a material configuration, the phenomena lead to potential permittivity or dielectric property increases within a thin semiconducting layer and gives much effect on the medium's dielectric states[5] that modulates the outcome of light scattering from and absorption in the particle. Concentrated energy confinement in localized plasmonic oscillations can be converted and transferred to the surrounding semiconducting medium to induce charge

separation with the change of dielectric properties. It is a result of conductive electron excitations at the interface between the metal particle surface and dielectric compounds. Therefore, SPR coupled with sufficiently large scattering cross sections of metallic NPs may scatter the incident light efficiently, enhance effective absorption cross sections, and locally amplify the electromagnetic field at the surface.[6] Therefore, these phenomena were applied in solar material composites and devices.[7−10]

We reported recently the observation of a large amplification of dielectric properties associated with the photoswitching effect and a new phenomenon of delayed photoinduced capacitor-like electric polarization behavior at the interface of three-layered core−shell (γ-FeO$_x$@AuNP)@[C$_{60}$(>DPAF-C$_9$)]$_n$ NPs at 0.5−4.0 GHz.[11,12] The structure of fullerene dyad C$_{60}$(>DPAF-C$_9$) **1**-C$_9$ is shown in Figure 1, where C$_{60}$> is an electron-acceptor (A) cage and DPAF-C$_9$ is an electron
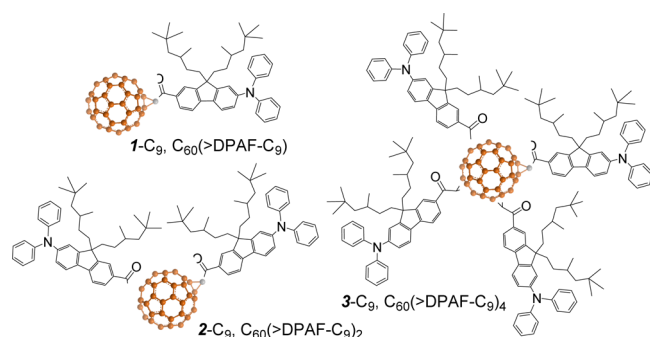
Figure 1. Compound structure of fullerene−chromophore conjugates as the monadduct **1**-C$_9$, the bisadduct **2**-C$_9$, and the starburst tetraadduct **3**-C$_9$.

donor (D) chromophore. These nanostructured NPs, consisting of an outer shell fullerosome layer derived from molecular self-assembly of e⁻-polarizable C$_{60}$-(light-harvesting donor antenna), were fabricated from highly magnetic core−shell γ-FeOx@AuNPs. Interestingly, energy-conversion and transfer from the accumulated SPR energy sites at the surface to the partially bilayered fullerosome membrane layer in a near-field (∼1.5 nm) were found to bear a close resemblance to the interpretation of concentrating or folding of the incident photon energy described above. By further engineering the number of light-harvesting donor antenna attached on a C$_{60}$> cage and having them deposited in the similar core−shell metallo-dielectric structures, we may be able to increase the light absorption and study the effect of SPR and surface-generated oscillating plasmon polaritons (polarized surface electrons) in interacting with C$_{60}$(>DPAF-C$_n$)$_x$-derived full-erosome layers.

Accordingly, we synthesized and performed permittivity or relative dielectric constant (ε_r') measurements of three magnetic core−shell hybrid samples of (γ-FeO$_x$@AuNP) @[C$_{60}$(>DPAF-C$_9$)$_x$]$_n$ **4**-D$_x$ [x = 1 (dyad), 2 (triad), or 4 (pentaad)] using **1**-C$_9$, C$_{60}$(>DPAF-C$_9$)$_2$ **2**-C$_9$, and C$_{60}$(>DPAF-C$_9$)$_4$ **3**-C$_9$ (Figure 1), respectively, as the e⁻-polarizable charge generators. Large reproducible and recyclable plasmonic dielectric amplification effects were detected in all samples of **4**-D$_x$ indicating the potential usage of these nanohybrids as promising photoswitchable RF-responsive materials for the study of tunability on reflective RF-signal images in the GHz frequency range.

2. EXPERIMENTAL SECTION

2.1. Synthesis of RF-Responsive Materials. Preparation of [60]fullerene monoadduct **1**, bisadduct **2**, and tetraadduct **3** followed the procedures reported previously.[13,14] Procedures for the fabrication of core−shell nanoparticles **4**-D$_x$ were based on those reported[11] recently with some modifications in details described in the Supporting Information.

2.2. Tunneling Electron Microscopic (TEM) Measurements. Both Formvar and carbon−copper film grids in a 200-mesh size were used for the topography investigation of molecularly assembled nanoparticle structures, derived from **1**-C$_9$ and **2**-C$_9$, by TEM images. Samples were prepared by directly coating the grid with a sample solution of 1.0 × 10⁻⁶ M diluted from the master nanoparticle solution (5.0 × 10⁻⁴ M in H$_2$O). Different concentrations (10⁻⁴−10⁻⁶ M) may be used and evaluated to ensure full separation of particles from each other without stacking prior to the collection of microimages. It

was followed by the freeze-dry technique via placing the sample-coated grid on a metal dish that was in thermal equilibrium with liquid nitrogen. This apparatus was then placed inside a vacuum chamber for overnight to remove all solvents completely prior to the measurement that will retain the nanoparticle shape on the grid. To prevent particle aggregations during the solvent removal procedure, a low concentration of 10⁻⁵−10⁻⁶ M in benzene is essential for the practice.

2.3. Dielectric Property (Permittivity or Relative Dielectric Constant ε_r') Measurements. Complex electric permittivity (F/m, including both terms of dielectric constant and loss factor) was carried out by an Agilent/HP E5071C Network Analyzer equipped with an open-ended Agilent/HP 85070E dielectric probe kit (200 MHz to 50 GHz). Calibration was conducted by using open-ended, close-ended, and attenuated calibrators prior to each measurement to remove the cable-related instability and system drift errors. A complex scattering parameter, defined as S$_{11}$, was measured and converted to complex electric permittivity values using Agilent/HP 85071E Materials Measurement Software with the experimental sequence depicted in the Supporting Information. This complex form is composed of a real and an imaginary part, which can be further converted to the dielectric constant and the loss factor. A custom-built chamber was applied for dielectric property measurements, conducted under a circumferentially uniform illumination environment. This is achieved by the installation of a reflective half-circular aluminum plate at the back-wall side surrounding the testing tube that is located at the center of the chamber. In this design, a light source was allowed to pass through a small window at the front side of the chamber to irradiate the sample tube. Reflected light beams are designed to refocus from the backside aluminum mirror plate back to the tube. Four fans were installed at the top and sidewalls of the chamber to control and prevent the temperature building-up inside the chamber.

A LED (light-emitting diode) white light with the output power of 2.0 W was used in the measurement as the illumination source. In a typical sample preparation, poly-(dimethylsiloxane) (PDMS) was applied as a polymer matrix host that is capable of forming a paste-like material with nanoparticles. A mixture of PDMS (1.0 g) and either γ-FeO$_x$ NPs **5** or γ-FeO$_x$@AuNPs **6** coated by **1**-C$_9$, **2**-C$_9$, or **3**-C$_9$ (100 mg) was prepared by dissolving all components in ethyl acetate (20 mL) in the testing tube under sonication until a clear solution was obtained. Ethyl acetate was then evaporated under vacuum to yield brown paste-like semisolid materials. A high amount of PDMS was used only in the concentration-dependent permittivity evaluations.

2.4. Distant Monostatic Reflective SAR image Measurements. A monostatic synthetic aperture RF-signal (SAR) measurement was performed using a triangular glass plate with or without the coating of (γ-FeO$_x$@AuNP)@[C$_{60}$(>DPAF-C$_9$)$_x$]$_n$ (coating thickness ∼1.0 mm) under illumination. Information contained in SAR images (e.g., shape and amplitude) was used for assessing the scattering response of an object, which is dependent on dielectric properties of the object. A symmetrical triangular glass plate in a dimension of 30 cm in base width and 32 cm in height was used. The coated area is a rectangle (5.0 × 6.8 cm) located at 8.0 cm down below the apex of the triangle, giving an approximate surface coated area of ∼7%. The SAR sensor carrying FMCW (frequency modulated continuous wave) signals has a carrier frequency of
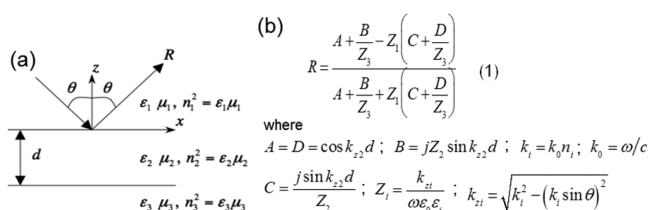
10 GHz with a bandwidth of 1.5 GHz and the range distance of 20 cm in all experiments. The measurement was controlled by an automated biaxial positioner to achieve accurate spatial registration of coordinates of the horn antenna. In rendering all SAR images, a standard strip SAR imaging mode with algorithm was applied.[15]

A sample of core–shell hybrid nanoparticle materials was coated on the triangle glass plate with a thickness of ∼1.0 mm in the measurement. The coating preparation was performed as follows. To a mixture of nanoparticle (100 mg) and PDMS (1.0 g) was added Sylgard 184 (100 mg, Dow Corning, containing a base of dimethylvinyl terminated dimethylsiloxane, dimethyl-vinyl and trimethylated silica, and tetra(trimethoxysiloxy)silane and a cross-linking cure agent of methylhydrogenated dimethylsiloxane copolymer and a palatinate catalyst, dielectric constant of 2.6−2.7). The mixture was whipped vigorously with a spatula for more than 30 min to ensure uniformly mixing of all the components. It was molded via coating on a glass plate which was placed horizontally after polymer setting. Since the whip-mixing procedure can produce many air bubbles, the glass plate was kept in a vacuum oven connected with a pump for 1.0 h at room temperature to remove the trapped air bubbles prior to the initiation of cross-linking reaction of Sylgard 184. The curing process was made by heating the coated glass plate at 80 °C for ∼60 min. Cured thin film sample on the plate became nonsticky and immobile.

2.5. Angle-Dependent Bistatic Reflective RF-Signal Imaging Measurements. A angle-dependent bistatic reflective RF-signal measurement was applied on either a triangular plexiglass plate or a semicircular casting iron plate with or without the coating of 4-D$_x$ NPs under illumination of the white LED light from the front side. Two doubly rigged horn antennas were positioned and coupled at the incidence of 10° with the reflectance for measuring the S21 scattering parameter of the object with or without light illumination. The object was installed on a rotary stage controlled by a digital controller (angular resolution of 0.1°) to achieve a precise angular increment. All RF-signal measurements were conducted at the frequency range of 0.5 to 18 GHz inside an anechoic chamber equipped with nonreflective wall-padding foams to eliminate the effect of electromagnetic background noise. Reflectivity of the object was measured by fixing the antenna pair configuration and rotating the rotary stage at either 0°, 15°, 30°, 45°, 60°, 75°, or 90° to develop a quantitative assessment of the angle-dependent scattering responses of the object with or without the coating of core−shell nanoparticles.

3. RESULTS AND DISCUSSION

3.1. Materials Design and Characterizations. In this study, RF-reflectivity of an object is defined as the reduction in the reflected power (the return loss in decibels) in a log-ratio to the incident power. The mode of electromagnetic (EM) wave propagation in a three-medium, two-layered material with a thickness of d follows those studied[16,17] that can be briefly depicted, as shown in Figure 2a. Incidence of a parallelly (p-) polarized transverse magnetic (TM) wave is reflected by the same incident angle (θ) at the surface of the material layer having the refractive index n_2. Reflection coefficient R can be determined by the eq (1) of Figure 2b, where k_i is the wavenumber, n_i is the refractive index, k_0 is the free space wavenumber, Z_i is the impedance of p-polarized TM wave, ω is the angular frequency, ε_o is the electric permittivity of free space (= 8.854×10^{-12} F/m), ε_i the relative complex

Figure 2. (a) Three-medium/two-layer model for the EM wave propagation and (b) the formula of reflection coefficient R.

permittivity (or dielectric constant) of the medium i. Therefore, RF-reflectivity can be modulated by the variation of relative complex dielectric constant (ε_r') of the material studied. This is consistent with the fact that the refractive index of a given medium is in a square-root relationship to the product of permittivity (ε) and permeability (μ). Both are relevant material parameters responsible for the tunability of EM waves passing through a medium. The former parameter is dependent on material's dielectric properties which can be correlated to the degree of electron (e^-) polarization at the frequency of measurements. It is especially valid for the case of nanostructures 4-D$_x$. One of our approaches is to maintain permeability of the material constant while operates on the tunability of permittivity by changing the disparity of e^--polarization in an ultrafast response rate. In principle, ferroelectric characteristics are derived from the spontaneous polarization of materials and the ordering of resulting electric dipoles in response to the external electrical field. It could be essential in this study to simulate the phenomenon of ferroelectricity as a means to increase or change the permittivity by the application of external energy.

Recently, we have demonstrated ultrafast intramolecular electron and energy transfer events in a nearly "spontaneous" rate of <130 fs (fs)[13] occurring in a conjugated A−(D)$_x$ system of fullerene−diphenylaminofluorene dyads $C_{60}(>DPAF\text{-}C_n)$ **1**-C$_n$,[18,19] triads $C_{60}(>DPAF\text{-}C_n)_2$ **2**-C$_n$, and pentaads[14,20,21] $C_{60}(>DPAF\text{-}C_n)_4$ **3**-C$_n$ by the femtosecond (fs)-laser irradiation measurements. In the former event, photoinduced e^--transfer from the DPAF-C$_n$ donor moiety to the $C_{60}>$ acceptor moiety resulted in the formation of a charge-separated (CS) transient state of $C_{60}{}^-\cdot(>DPAF^{+\cdot}\text{-}C_n)_x$ in a long lifetime of ∼900 ns, in the case of **3**-C$_9$.[20] The observed ultrafast photoresponsive rate was rationalized by the concurrence of keto−enol tautomerism[12] leading to periconjugation at the bridge unit between $C_{60}>$ and the carbonyl moiety of DPAF-C$_n$ in a spacing distance of only ∼3.5 Å, as verified by X-ray single-crystal structural analysis of **1**-C$_2$.[13] Therefore, it is rational to apply these analogous C_{60}-(light-harvesting antenna)$_x$ conjugates as charge generators to become effective upon excitation by the external energy.

Synthetic sequence of the core−shell nanoparticle preparation is depicted in Figure 3. Similar synthetic sequence and procedures to those reported with slight modifications were applied for the preparation of [60]fullerene adducts **1**-C$_9$,[22] **2**-C$_9$,[22] and **3**-C$_9$.[14] Fabrication of bilayered core−shell NPs (γ-FeO$_x$@AuNP, **6**) with highly magnetic γ-FeO$_x$ (**5**, 1.0 < x < 1.5) NPs as the nearly monodisperse nanocrystalline[23] core material was made by using the combined method described recently.[11] To make a consistent evaluation of plasmonic properties of the Au layer, the same weight ratio of the precursor reagent HAuCl$_4$·3H$_2$O to the quantity of iron oxide NPs was applied. Surface of the resulting gold layer was
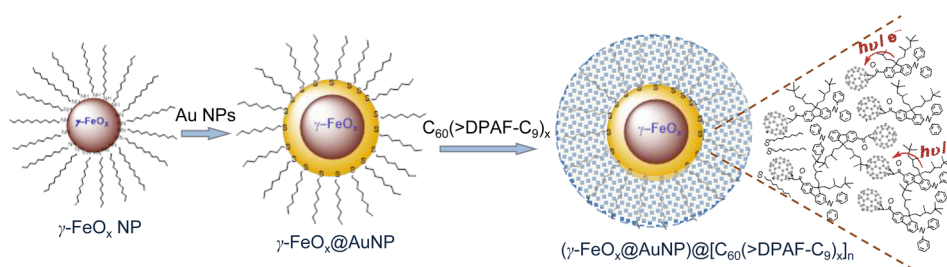
Figure 3. Schematic description of core−shell nanoparticle preparation sequence.

stabilized by 1-octanethiol as a capping agent in sufficient binding to render moderate solubility of NPs in toluene that facilitated the subsequent encapsulation by $C_{60}(>DPAF-C_9)_x$. Purification of core−shell NPs was carried out by the use of an external magnet to retrieve and isolate only the magnetic NP solids and separate out any possible nonmagnetic Au-NP byproduct formed during the preparation. Encapsulation of **6** by either **1**-C_9, **2**-C_9, or **3**-C_9 was performed under ultrasonication in toluene to replace surface-bound 1-octanethiol by C_{60}-adducts that resulted in the formation of trilayered core−shell $(\gamma$-FeO$_x$@AuNP)@$[C_{60}(>DPAF-C_9)_x]_n$ **4**-D_x (x = 1, 2, or 4) NPs. Ligand exchange was effective in a concentrated solution via sonication to increase the molecular contact of **1**−**3** to NPs **6**. With assistance of an external permanent magnet, the procedure made the removal of residual capping agents and an excessive amount of $C_{60}(>DPAF-C_9)_x$ on surface easy by repeated rinsing with ethanol and ether. The ability of **1**−**3** to replace 1-octanethiol on a gold surface relies on strong C_{60} bonding interactions to metal or the gold surface[24] in the form of a monolayer.[25] Similar examples were demonstrated by one fullerene monoadduct PCB-capped gold nanoparticles.[26,27] In the presence of both sulfur-ligands and C_{60} cages, their surface binding forces to Au can be competitive to each other for attaching to chemisorption sites with the surface binding energy of C_{60}−Au calculated to be higher than the Au−S bond strength.[28] This makes the alkylthiol−C_{60} exchange equilibrium shift more favorably toward the effective attachment of C_{60} cages to Au. In addition, multilayered self-assembly formation of fullerene derivatives may also be possible owing to strong fullerene−fullerene and fullerene−gold interactions.[29]

Under our experimental conditions, application of the ultrasonication energy was able to dissociate the S−Au interactive binding that allowed $C_{60}(>DPAF-C_9)_x$ (x = 1 or 2) to penetrate the 1-octanethiol layer and intercept chemisorption sites. It was then followed by the strong hydrophobic−hydrophobic interaction forces of $(C_{60}>)$−$(C_{60}>)$ cages that may favor monolayer molecular self-assemblies of $C_{60}>$ at the gold surface. This should push weaker Au-interactive DPAF-C_9 ring moieties outward with 3,5,5-trimethylhexyl chain moieties phasing the solvent. Subsequent packing of fullerene dyads, by keeping the same preference of $(C_{60}>)$−$(C_{60}>)$ and aliphatic−aliphatic interactive forces, would lead to a partial bilayer or bilayer packing configuration of **1**-C_9 or **2**-C_9 at the outer surface. This structure resembles that reported on nanovesicles of amphiphilic $C_{60}(>DPAF-EG_x)$ conjugates showing bilayered fullerosome (ordered $C_{60}>$ assemblies) membrane spheres,[30] as detected by tunneling electron microscopic (TEM) micrographs.

We carried out the core−shell morphology, size, and layer-thickness investigation of all NPs **5** and **6** used in the

preparation of **4**-D_x by TEM measurements using the average particle size of parent γ-FeO$_x$ NPs determined in their micrographs as the reference for comparison. A highly homogeneous particle size distribution of NPs **5** used in this study was observed in Figure 4A, with an average particle size
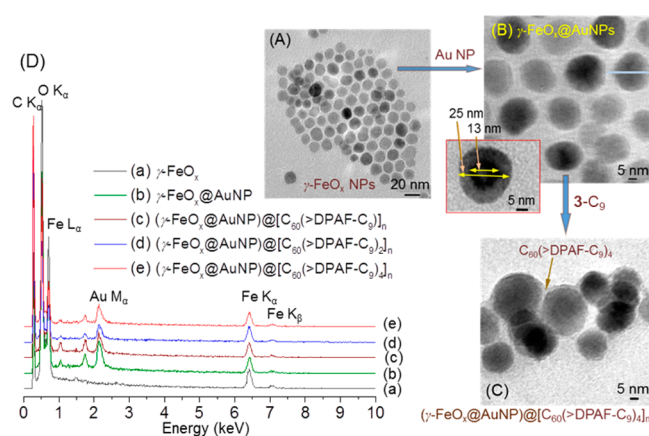

Figure 4. TEM micrographic images of (A) γ-FeO$_x$ **5**, (B) γ-FeO$_x$@AuNP **6**, and (C) trilayered core−shell **4**-D_4 NPs, showing evolution of particle morphology changes. (D) Energy dispersive X-ray spectra (EDS) of (a) **5**, (b) **6**, (c) **4**-D_1, (d) **4**-D_2, and (e) **4**-D_4, showing the relative intensity of compositional elements where the carbon of (a) and (b) arises from the carbon tape used for the sample preparation and the oxygen of all materials was from both the sample and the environment.

measured around 12−14 nm in diameter in a rather narrow distribution. Subsequent chemical reduction of HAuCl$_4$ to effect the deposition of a gold layer increased the diameter of many particles to 21−25 nm (Figure 4B), also in a narrow distribution. Most of γ-FeO$_x$@AuNPs **6** displayed a slightly lighter contrast difference at the edge layer with one particle (the inset of Figure 4B) showing a clear boundary between the darker γ-FeO$_x$ core region and the lighter Au layer making it possible to measure the iron oxide core diameter of ∼13 nm and the Au layer thickness of ∼6.0 nm. Further deposition of **3**-C_9 at the outer shell led to encapsulation of many nanoparticles by a layer of organic substance in light and soft amorphous images (Figure 4C). It was estimated by a shell thickness of 5−7 nm in the sample of **4**-D_4. By using the MM2 energy minimization technique to simulate the 3D molecular configuration with the assumption of a C_{60} cage diameter width being 1.0 nm, we estimated a molecular sphere diameter of starburst-shaped **3**-C_9 in roughly 4.5 nm. This fits well with the overlap of two **3**-C_9 molecules to match with an observed partial bilayer packing thickness of the outer shell layer. In the case of the dyad **1**-C_9 or the triad **2**-C_9, a partial bilayered or bilayered fullerosome membrane packing consisting of a head

(C_{60}>)-to-head (C_{60}>) orientation of dyads or triads on the surface of γ-FeO$_x$@AuNP was proposed.[11] It is conceivable to assume the molecular packing orientation based on strong attraction forces between the C_{60}> cage and AuNP discussed above.

We confirmed the elemental composition of nanoparticles 4-D$_x$, **5**, and **6** by using microanalyses of energy dispersive X-ray spectra (EDS) of these NPs, performed on a JEOL JSM 7401F Field-emission scanning electron microscope equipped with a EDAX Genesis XM2 Imaging System. As a result, in the absence of detectable Au particles in the image, intensity of observed Fe and Au peaks in the spectra of **6** (Figure 4D-b) can be accounted for a molar ratio (Fe:Au) of 10.8:1. The spectrum substantiated the coating of a thin Au layer on γ-FeO$_x$ NPs consistent with the nanoparticle images appeared in Figure 4B, by the comparison between Figure 4D-a and D-b, whereas the molar ratio of C:Fe:Au of trilayered 4-D$_1$ (Figure 4D-c), 4-D$_2$ (Figure 4D-d), and 4-D$_4$ (Figure 4D-e) were measured to be 63.1:16.2:1, 70.6:19.9:1, and 65.4:16.5:1, respectively. A higher Fe:Au ratio than that of **6** may reveal a certain degree of core–shell thickness variation of Au during a different batch of preparation. However, the C:Fe ratios were roughly constant within the error of estimates among three core–shell samples 4-D$_x$ indicating a good reproducibility in deposition of C_{60}(>DPAF-C$_9$)$_x$ in quantity and fullerosome thickness using the current fabrication procedures.

In the molecules of C_{60}(>DPAF-C$_9$)$_x$, two photoresponsive moieties of C_{60}> and DPAF-C$_9$ chromophore were linked together by a cyclopropanylketo group with a highly acidic α-proton at the junction. Facile relocation of this proton to carbonyl oxygen facilitates the keto–enol tautomerism chemistry along the bridging unit that increases the partial conjugation length in the enol form between the C_{60}> acceptor and the DPAF-C$_9$ donor. The isomerization broadens optical absorption bands of both C_{60}>, centered at 326 nm, and DPAF centered at 400–410 nm (Figure 5a–c and e). By increasing
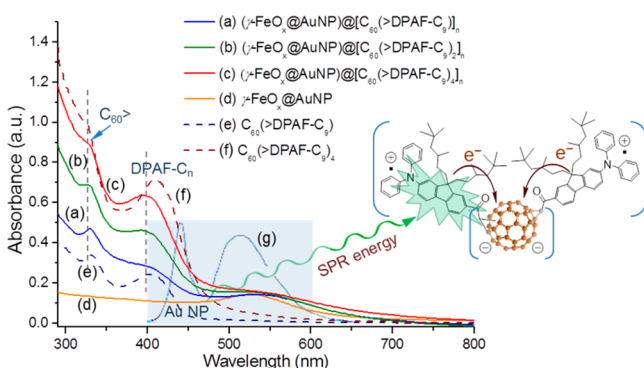

Figure 5. UV–vis absorption of (a–c) 4-D$_1$ in CHCl$_3$–THF (1:5), (d) γ-FeO$_x$@AuNP stabilized by n-C$_8$H$_{17}$SH, (e) **1**-C$_9$ in CHCl$_3$, and (f) **3**-C$_9$ with their absorption correlation to emission bands (in light blue rectangle) of white LED light used.

the number of DPAF units per C_{60}> to four in **3**-C$_9$ and 4-D$_4$, the absorption extinction coefficient (ε_{ab}) at 410 nm was multiplied (Figure 5f and c, respectively) that also raised the ε_{ab} value at 350 nm, attributing to overlap with the cage moiety. Optical absorption spectrum of the AuNP subshell layer displayed a broad profile (Figure 5d) over the entire wavelength range with the band maximum centered around 550 nm. Therefore, it easily gives absorption overlap with those

of **1**-C$_9$, **2**-C$_9$, and **3**-C$_9$ that makes the interlayer energy transfer efficient. The amount of LED light photons to be captivated at the surface is dependent on the shape morphology, particle size, and thickness of the AuNP layer and the DPAF quantity with absorption wavelengths in overlap with the emission wavelength and intensity of the LED light at 400–600 nm, as shown in the light blue shadow area of Figure 5.

Fullerenes are highly electronegative cages. It is capable of taking electrons from the gold surface via strong interactions forming a reduced charge state.[31] By increasing the fullerene concentration in the lipid membrane, a photocurrent was detected indicating the event of electron-transport among negatively charged C_{60} via hopping.[32] Similar phenomena could be expected on the system of 4-D$_x$ having a fullerosome membrane upon photoexcitation at the gold surface. Combination of all these events including initial SPR energy generation, followed by facile induction and production of fullerenyl negative charges and, then, facilitating subsequent charge transport in fullerosomes together may lead to synergic effects on enhancement of dielectric properties. In the former event, sufficient interactions of LED light's EM field in the Au layer were known to induce a collective coherent oscillation of conducting free electrons at the gold surface acting as an oscillating dipole along the direction of the electric field.[3] It leads to surface plasmon charge density fluctuation of polaritons in amplitude as resonance at the interface between AuNPs and dielectrics. This photoinduced SPR energy generated can be subsequently transferred to C_{60}(>DPAF-C$_9$)$_x$ dielectrics in a near-field giving the induced intramolecular e$^-$-transfer from one or two DPAF donor moieties to C_{60}> in the case of 4-D$_1$ or 4-D$_2$ (as **2**-C$_9$ in the inset of Figure 5), respectively. An example of similar SPR energy transfer in the core–shell nanoparticle materials was observed at the interface of Au and semiconductor layers.[33] In the event of a bilayer or partial bilayer fullerosome membrane layer formation at the outer-shell layer of 4-D$_1$ or 4-D$_2$ by self-assembly of **1**-C$_9$ or **2**-C$_9$ molecules, respectively, the phenomena of e$^-$-transfer leads to a charge-separated transient state of $C_{60}^{-\bullet}$(>DPAF$^{+\bullet}$-C$_n$) for 4-D$_1$ or C_{60}^{-2}(>DPAF$^{+\bullet}$-C$_n$)$_2$ for 4-D$_2$. As discussed above, fullerosome consists an array of C_{60}> cages in the membrane. The negative charges should be concentrated at the cage area while the positive charges will be distributed along the DPAF assemblies, giving the charge polarization within the fullerosome membrane. This was correlated to the detected dielectric amplification in the measurement discussed below.

3.2. Permittivity and Dielectric Investigations. Permittivity and dielectric properties of (γ-FeO$_x$@AuNP)@[C_{60}(>DPAF-C$_9$)]$_n$ 4-D$_x$ were investigated in measurements carried out using an open-ended coaxial probe and a network analyzer in the frequency range of 0.5–4.5 GHz. Elucidation and conversion of measured scattering parameter (S$_{11}$) data provided information on the relative dielectric constant (ε_r', the real part of complex permittivity) and the relative dielectric loss factor (ε_r'', the imaginary part of complex permittivity). For comparison purposes, several samples were first evaluated to establish the reference values. They included C_{60}(>DPAF-C$_9$) alone, γ-FeO$_x$ **5** nanoparticles alone, γ-FeO$_x$@[C_{60}(>DPAF-C$_9$)]$_n$ NPs, and γ-FeO$_x$@AuNP **6** in PDMS as a mixture to show either none or insignificant changes of ε_r' under both switch-on and switch-off irradiation conditions. We selected a LED white light with the output power of 2.0 W for the study. Under the emission wavelength range and the band intensity of
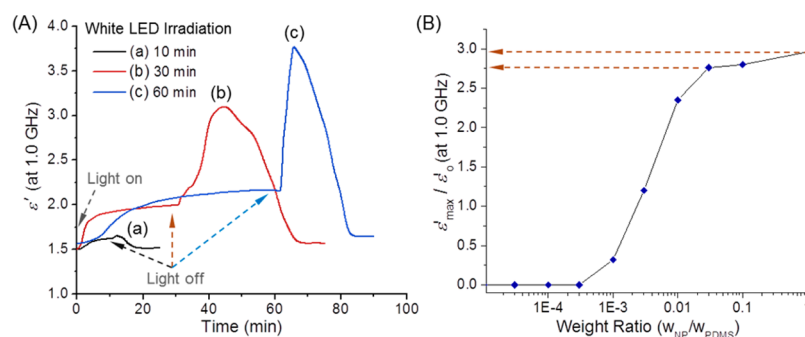
Figure 6. (A) Irradiation fluence-dependent relative dielectric constant (ε_r') amplification of core−shell (γ-FeO$_x$@AuNp)@$[C_{60}(>\text{DPAF-C}_9)]_n$ **4-D$_1$** without PDMS at the RF frequency of 1.0 GHz. Irradiation period was (a) 10, (b) 30, and (c) 60 min. (B) Concentration-dependent relative ε' value of **4-D$_1$** in PDMS.
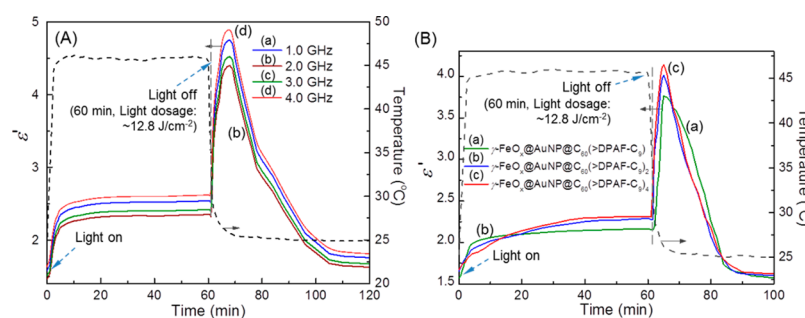

Figure 7. Large sharp relative dielectric constant (or permittivity) amplification of (A) (γ-FeO$_x$@AuNP)@$[C_{60}(>\text{DPAF-C}_9)]_n$ **4-D$_1$** in a mixture with PDMS (1:10 by wt.) detected by the data taken at different frequencies (1.0−4.0 GHz) and (B) **4-D$_1$**, **4-D$_2$**, and **4-D$_4$** prepared by a different batch of core−shell formation from those of (A) for comparison at 1.0 GHz. Both (A) and (B) used a collimated LED white light showing rapid switch-on increase of ε_r' at the light-off stage after 60 min irradiation.

a white light (blue shaded area of Figure 5), the emission spectrum matched with optical absorptions of the gold layer over the full range and a part of DPAF-C$_9$ moiety at 415−450 nm, indicating the main photoexcitation processes occurring at these two components. The absorption peak of the C$_{60}$> cage with a maximum (λ_{max}) centered at 326 nm is outside the range. Therefore, it should not be involved directly in initial photoexcitation events.

Several permittivity measurements were conducted inside a custom-built chamber to create a circumferentially uniform illumination environment. Its inner chamber temperature was maintained and controlled using several fans to minimize heat building up, showing only a small increase from 25 to 45−46 °C (right y-axis of Figure 7) when the light was turned on for a period of 60 min. The chamber temperature dropped quickly back to 25 °C after light-off. In the study, illumination periods were chosen to be 10, 30, and 60 min giving the corresponding light fluence of 2.13, 6.41, and 12.8 J/cm^2, respectively. As a result, interestingly, the quantity of relative dielectric constant amplification collected on core−shell nanoparticle materials **4-D$_1$** without PDMS at the RF frequency of 1.0 GHz (Figure 6A) was found to be highly dependent on the quantity of irradiation fluence. At a low fluence accumulated over a period of 10 min (Figure 6A-a), insignificant changes of ε_r' at the light-off stage were detected. When the light fluence was accumulated over a period of 30 min (Figure 6A-b), a large increase of ε_r' with the profile showing as a broad band at the light-off stage was observed. The peak ε_r' at maximum (ε_{max}') value of 3.09 at the light-off stage represented a 206% increase from $\varepsilon_r' = 1.5$ at the time zero. Upon further increase of the accumulated light fluence to 12.8 J/cm^2 (Figure 6A-c), a much sharper jump of ε_r'

quantity was noticed immediately after turning off the light. Its peak maximum ε_{max}' value of 3.63 corresponds to an amplification of 242%. The data strongly support our hypothesis that the molecular polarization of C$_{60}(>\text{DPAF-C}_9)$ is SPR energy-induced and the polarized charge quantity in the fullerosome layer is dependent on the accumulated total SPR energy.

To facilitate or enable the use of **4-D$_x$** in the film coating process, we investigated the concentration-dependent relative ε' value of **4-D$_1$** in PDMS polymers with the results shown in Figure 6B. Soft elastic property of PDMS as a polymer host was able to provide a tight packing in filling up air-gaps among particles after solvent evaporation that is critical for eliminating the air contribution to the ε_r' value obtained. Its dielectric constant is comparable in value to that of C$_{60}(>\text{DPAF-C}_9)$. Variation of the nanoparticle **4-D$_1$** concentration in PDMS was estimated in terms of the weight ratio as W_{NP}/W_{PDMS} based on the consistent amount of **1-C$_9$** per unit weight (mg) of NPs applied in the preparation of core−shell materials. At a low ratio of 2×10^{-4}, nearly no detectable ε_r' was found, as shown in Figure 6B. By increasing the weight ratio above 10^{-3} to 10^{-2}, the measured magnitude of $\varepsilon_{max}'/\varepsilon_o'$, where ε_o' is ε_r' at the time zero and ε_{max}' is the maximum ε_r' after 60 min irradiation, sharply surged from 0.26 to 2.31. The curve ascending slop became smaller above the weight ratio of 0.03 and 0.1 giving the $\varepsilon_{max}'/\varepsilon_o'$ values as 2.75 and 2.76, respectively, which is close to the $\varepsilon_{max}'/\varepsilon_o'$ magnitude of nearly neat **4-D$_1$** as 2.95. Therefore, we select a ratio of W_{Np}/W_{PDMS} as 1:10 to be an optimal mixture composite to maintain a good viscosity and the film strength of the sample mixture for coating applications and
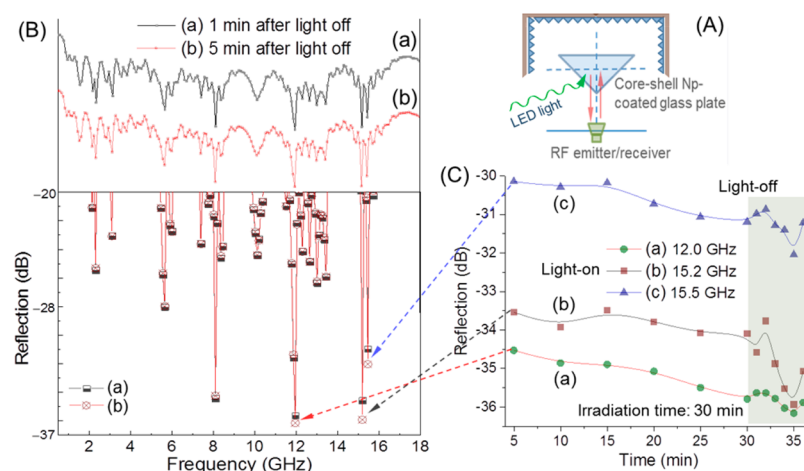
Figure 8. (A) Experimental setup of monostatic RF-reflection measurement. (B) Frequency-dependent reflectivity of **4**-D_1 coated glass plate at (a) 1.0 min and (b) 5.0 min after 30 min (1.3 J/cm^2) front illumination by a LED white light and (C) time-dependent curve profiles of reflection at three specific frequencies to show the change (marked by light green) of reflectivity at the light-off stage at 30−38 min.

to balance a minimum reduction of the ε_r' signal as compared with that of the neat **4**-D_1.

Frequency-dependent permittivity measurements were also performed under a similar experimental setup and conditions described above. The reflected signal was evaluated in terms of ε_r' and relative loss factors (ε_r'') at 0.5−4.5 GHz under illumination with a LED white light. Figure 7 shows relative dielectric constant (or permittivity, ε_r') curve profiles of **4**-D_1 NPs in PDMS (1:10 by wt.) with the data taken at different frequencies (1.0−4.0 GHz) during and after 60 min illumination using a collimated white LED light. Total accumulated light fluence over a period of 60 min was 12.8 J/cm^{-2}. The initial increase of ε_r' measured from the time zero to the time 5 min matched well with the sharp surging profile of the chamber temperature from 25 to 47 °C, indicating increased ε_r' magnitudes from the time zero value to 2.34, 2.40, 2.47, and 2.59 at 2.0 (Figure 7A-b), 3.0 (Figure 7A-c), 1.0 (Figure 7A-a), and 4.0 (Figure 7A-d) GHz were owing to the chamber-related thermal effect. These magnitudes remained relatively steady over the illumination period of 20 to 60 min. Shortly after the light being turned off, we observed an interesting rapid upsurge of permittivity to a maximum magnitude of 4.34, 4.50, 4.72, and 4.88 at 2.0, 3.0, 1.0, and 4.0 GHz, respectively, reached at roughly 7.0 min after the start of light-off state. These permittivity magnitudes correspond to a ratio of $\varepsilon_{max}'/\varepsilon_o'$ ($\varepsilon_o' = 1.58$ at the time zero) in a roughly 2.75-, 2.85-, 2.99-, and 3.09-folds at the peak maximum for 2.0, 3.0, 1.0, and 4.0 GHz, respectively. Extent of the photoswitchable dielectric amplification on permittivity was the highest that we have observed to date, especially, on the samples at the frequency of 4.0 GHz. The comparison was made with our fullerenyl monoadduct nanomaterials reported recently,[11,12] the only examples available. Since no detectable changes of ε_r' values were observed during or after the irradiation period (60 min) with the samples of **1**-C_9, γ-FeO$_x$ NPs, and core−shell γ-FeO$_x$@[C_{60}(>DPAF-C_9)]$_n$ NPs (without Au) measured at 1.0 GHz, observed amplification phenomena of ε_r' can be correlated solely to the influence of the gold layer of **4**-D_x after light illumination. As discussed above, it is owing to the generation of plasmon-energy at the surface which was photoinduced by the light applied.

As the number of e$^-$-donor chromophore per $C_{60}>$ increases from 1 to 2 and 4 in the conjugates **2**-C_9 and **3**-C_9, respectively, the corresponding core−shell NPs **4**-D_2 and **4**-D_4 exhibited similar phenomena of dielectric amplification at the permittivity maximum in less than 7.0 min after the light being turned off, as shown in Figure 7B. It was then followed by a relaxation process of ε_r' back to a value of 1.57 nearly identical to the initial ε_r' value, indicating a good recyclability of photoswitching characteristics in light-on and light-off cycles. By considering a nearly identical dielectric constant among **4**-D_1, **4**-D_2, and **4**-D_3 at the time zero, the maximum permittivity magnitude of 3.76, 4.0, and 4.14, respectively, at the time of 67 min indicated a 6.4 and 10% increase of ε_r' for **4**-D_2 and **4**-D_3, respectively, from that of **4**-D_1. We have previously demonstrated the phenomena of efficient photoinduced intramolecular charge separation of **2**-C_9 and **3**-C_9 in polar media using nanosecond transient spectroscopic measurements.[20] Photoexcitation processes resulted in the formation of corresponding transient CS state of these nanomaterials consisting of a positively charged (DPAF-C_9)$^{+\bullet}$ and a negatively charged ($C_{60}>$)$^{-\bullet}$. With the increase of the number of DPAF-C_9 antenna moieties attached per $C_{60}>$ cage to 4, the CS transient state lifetime (τ_{CS}) was found to be prolonged, sufficiently long enough for its contribution to permittivity properties. Therefore, we considered the generation of these CS states within the outer shell layer of **4**-D_x NPs being the source of electric charges to amplify the observed permittivity in RF frequency range.

3.3. Synthetic Aperture RF-Signal (SAR) Measurements. We applied the above stated photoswitchable dielectric amplification effect toward the tunability and switching capability study of distant monostatic reflective RF-signal image modulations to provide certain insights to our study of RF-signal tunable coating applications. They were performed by a monostatic SAR measurement of a triangular glass plate with or without the partial coating of **4**-D_1 NPs in PDMS as a thin film on a glass plate under front LED-white illumination for a defined period of time. In this measurement scheme, only one RF antenna horn is needed, as shown in Figure 8A. We first examined the sample reflectivity, defined as the reduction in reflected power in decibels (dB) by the relationship of log(P_i/P_r), where P_i is the incident power and P_r is the reflected power,
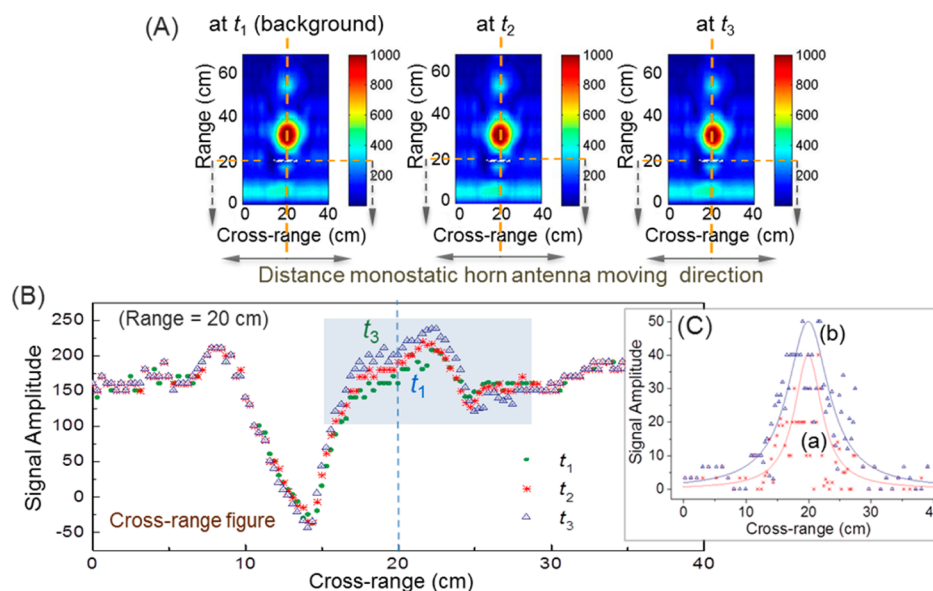
Figure 9. (A) Distant monostatic SAR images (where the central red spot was the image of a back-light unit) and (B) the cross-range RF-signal amplitude of a **4-D$_1$**-coated triangular glass plate collected at the range distance of 20 cm with or without LED-white back-light illumination, where t_1 with no light; t_2 with 15 min of irradiation, and t_3 with 30 min of irradiation at 10 GHz. (C) Calculated signal changes by the difference of (a) $|t_2 - t_1|$ and (b) $|t_3 - t_1|$, showing fluence-dependent change amplitudes.

at the light-on and light-off stages. Figures 8B-a and 8B-b displayed the frequency-dependent reflectivity curve profiles over 1.0−18 GHz at 1.0 and 5.0 min, respectively, after turning off the light. The total accumulated light fluence was measured to be ~1.3 J/cm^2. Magnitude of reflection changes was not uniform over the full frequency range. We arbitrarily selected three frequencies at 12.0 (Figure 8C-a), 15.2 (Figure 8C-b), and 15.5 (Figure 8C-c) GHz as examples to demonstrate their time-dependent reflection characteristics that covered an illumination period of 30 min and a period of 8.0 min at the light-off stage. During the light-on stage, magnitude of reflection curves derived from these three frequencies was relatively smooth with no significant fluctuation. Immediately after the light being switched off, clear reflection fluctuations were detected by an initial increase at the time 30−32 min followed by a decrease to a minimum at the time 35 min in a similar manner for all three curve profiles. Among them, RF reflectivity responses at 15.2 GHz were measured to be larger. This demonstrated that the magnitude of reflectivity change may be frequency-dependent with more at one frequency than the others. The data are found to be consistent with photoswitching phenomena discussed in Figure 7 even though a much shorter illumination period was applied.

In the case of distant monostatic SAR measurement, via scattering parameter S11, on a similar triangular glass plate partially coated by **4-D$_1$** NPs in PDMS, the SAR sensor bearing a carrier frequency at 10 GHz and a bandwidth of 1.5 GHz with FMCW (frequency modulated continuous wave) signals was used in the experiment. Both electrical and magnetic properties were accounted in the measurement. It is controlled by an automated two-axis positioner to achieve accurate spatial registration of coordinates of the horn antenna. RF-signal scanning is conducted in both vertical and horizontal directions to render the scattering imagery (or RF-signal imagery) of the target. RF-signal images of a triangular glass plate with or without any coating were scanned in either horizontal and or vertical directions for comparison. Information contained in SAR images (*e.g.*, shape, amplitude) can be used for assessing

the scattering response of an object, which is dependent on the object's dielectric properties. We determined the geometry of the triangular glass plate first. The same glass plate was subsequently partially coated in an area dimension of 5.0 × 6.8 cm (as a 7%-area of the plate) with (γ-FeO$_x$@AuNP) @[C$_{60}$(>DPAF-C$_9$)]$_n$ **4-D$_1$** nanoparticle-derived thin film using PDMS as a matrix material. The total signal reflectivity measured under the condition without or with a defined back-light irradiation period was counted to indicate the overall response to signal profile changes. Integrated RF-signal scattering response was represented by the spatial distribution (range vs cross-range) of SAR amplitude indicating the combined effect of dielectric property, surface roughness, size of NPs-coated area, and inspection angle. We used the collected responses at t_1 (Figure 9A, without irradiation) as the reference baseline. Two reflectivity amplitude peak profiles and photo-induced intensity changes over the range (r, vertical direction) and cross-range (r_x, horizontal direction) distance in measurements were evaluated for the signal comparison via illumination ($h\nu$) by a LED-white light for a period of 15 (t_2) or 30 (t_3) min (Figure 9A). To better assess the effect of dielectric amplification upon light illumination, cross-range SAR amplitude curves were extracted at the range distance $r = 20$ cm and shown in Figure 9B. As a result, photoinduced dielectric amplification of **4-D$_1$** was observed with the cross-range SAR amplitude curve displaying the relationship of $I(t_3$, 30 min $h\nu) > I(t_2$, 15 min $h\nu) > I(t_1$, 0 min $h\nu)$ at $r_x = 20$ cm, as an example. The main RF-response deviation area was found to be focused at the vicinity of the coated sample zone located at the cross-range distance of 20 cm (marked by a dash line in Figure 9B). To assist the visualization of the changing magnitude, we calculated signal changes by the difference of amplitude $|t_2 - t_1|$ and $|t_3 - t_1|$ and having the results plotted in Figure 9C-a and C-b, respectively. By using a curve fitting technique over largely scattered data points, the trend of the plotted $|t_3 - t_1|$ band became clearly shifting upward from that of Figure 9C-a to C-b. It revealed a positive deviation of RF-signals in amplitude as observed in the cross-range of 12−27
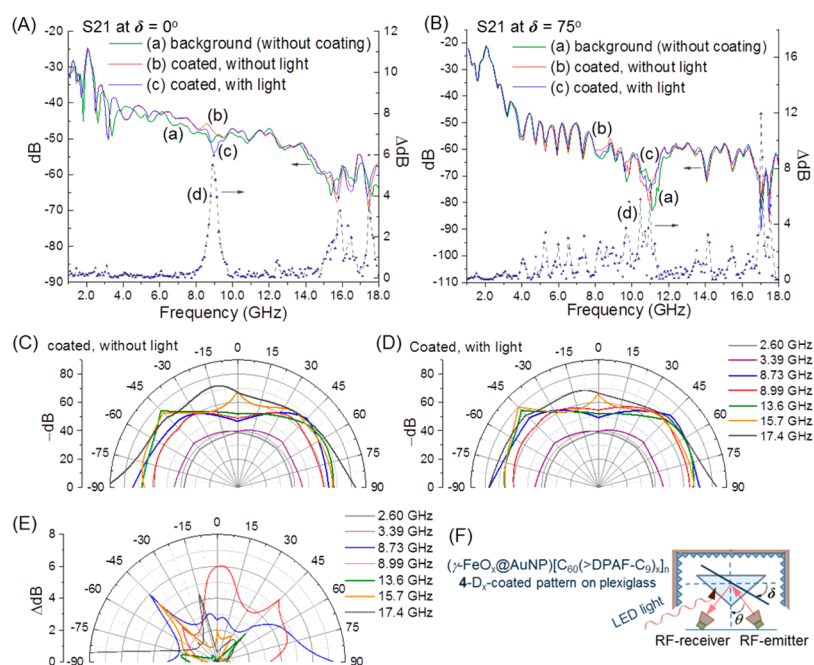
Figure 10. Frequency-dependent S21 scattering parameter based reflectivity (dB) of 4-D_1 in PDMS coated rectangular pattern on a plexiglass plate at the δ angle of (A) 0° and (B) 75° with or without the front illumination by a LED white light. The light-induced differences or changes (ΔdB) is calculated by |(D) − (C)|. Angle (δ)-dependent RF-reflection at seven different frequencies selected from (A) or (B) under conditions of (C) no light and (D) 30 min of front illumination (1.3 J/cm²). (E) Calculated difference (ΔdB) by |(D) − (C)| and (F) experimental setup of bistatic RF-reflection measurement with two horn antenna.

cm with the progressive increase of changes in a light fluence-dependent manner as exhibited by $|t_3 − t_1| > |t_2 − t_1|$, indicating higher values for a 30 min irradiation (4.0 J/cm² fluence) than those with 15 min irradiation (2.0 J/cm² fluence) or no light (zero fluence). In addition, total accumulative reflective signal amplitude increase ratios $(|t_2 − t_1|)/t_1$ and $(|t_3 − t_1|)/t_1$ integrated over the full cross-range of 0−40 cm were found to be 2.01 and 6.92%, respectively. Since the coated area ratio $A_{coated\ area}/A_{total\ area}$ was ∼0.07, the effective SAR amplification ratios $[(|t_2 − t_1|)/t_1]_{effective}$ and $[(|t_3 − t_1|)/t_1]_{effective}$ were calculated to be 29.5 and 99.1%, respectively.

We also carried out bistatic scattering parameter S21 measurements, with the setup scheme depicted in Figure 10F using one emitter and one receiver horn antenna, positioned at 90° (θ = 45°) to each other, to substantiate the application feasibility. The reflectivity data were collected on a partially coated triangular plexiglass plate by 4-D_1 in PDMS at the frequency range of 1.0−18 GHz and two inspection angles (δ = 0° and 75°) with or without the front illumination. Selection of these two angles was arbitrary for the demonstration purpose of angle-dependent characteristics. At 0° incidence (Figure 10A), partial coating with 4-D_1−PDMS significantly increased or reduced scattering responses of the target by roughly ±2.0−3.5 dB (ΔdB, defined as the difference or change between Figure 10A-b, A-c, and A-a) at the frequency range of 2.5−9.5 and 15−17.5 GHz, considering only ∼7% of coated area applied. A slightly lesser extent of 0.5−1.5 dB in changes was detected over the other frequency range of 1.0−2.0 and 10−15 GHz. When the incident angle was increased from 0° to 75°, main signal deviation areas shifted to the frequency range of 9.5−12 and 16.5−17.8 GHz (Figure 10B) with the spectrum profile of the rest of the frequency ranges remaining relatively similar among all three conditions taken. Different spectral profiles obtained might be due to the surface roughness of uncoated

metal plate in a rather small size that resulted in drastic increase or reduction of S21 values during the bistatic data collection. This implied that photoinduced effects leading to signal amplitude alternation of the scattering response and reflectivity may not be homogeneous throughout various frequencies. For example, S21 parameter values by the incidence horn angle of 0° decreased (the shielding effect induced by photoexcitation) in frequency ranges of 8.0−9.7 and 16.5 GHz, but increased at 15.7 and 17.4 GHz when compared by the ones with or without light illumination. Therefore, we selected some of these frequency ranges to investigate their angular scattering responses using the same partially 4-D_1/PDMS-coated plate sample. Results were displayed in Figure 10C (without light) and D (with 30 min illumination and a total fluence of ∼1.3 J/cm²). All frequencies higher than 3.5 GHz gave appreciable signal profile changes over the most of angular range. As these angle-dependent illumination-induced reflective signal changes (ΔdB) by |(D) − (C)| were plotted over 0°−(±90°) with the value shown in Figure 10E, we noticed that all curve profiles displayed a rather clear image of reflectivity variation over all inspection angles. Among them, reflectivity changes at 8.73, 8.99, 15.7, and 17.4 GHz were the most pronounced in photoresponses. They all responded in their own unique manner at each selected inspection angle. It is interesting to note that a small frequency variation from 8.73 to 8.99 GHz can lead to significantly large differentiable changes in photo-responses at different angles, indicating a high frequency-dependent sensitivity involved. Since this particular frequency range is used for maritime and aeronautical mobile communications, appreciable photoswitching tunability of reflective signals by 4-D_x could have implication in the corresponding applications.

4. CONCLUSION

We applied both branched and starburst C$_{60}$-DPAF multi-adduct conjugates to demonstrate the tunability of RF-responses by the generation of photoinduced surface plasmonic resonance effects on trilayered core−shell nanoparticles consisting of a highly magnetic γ-FeO$_x$@AuNP core and e$^-$-polarizable C$_{60}$-DPAF adduct-derived partially bilayered fullerosomes as the shell layer materials. Owing to the fact that there were nearly no dielectric changes on several nanoparticle samples without Au, observed large dielectric (permittivity) amplification phenomena were correlated and associated directly to the photoactivation of the gold layer. The event caused the induced excitation within C$_{60}$(>DPAF-C$_9$)$_x$ components. It is noteworthy to point out that the measured permittivity of 4-D$_x$ only reflects the ε_r' value of 1-C$_9$, 2-C$_9$, or 3-C$_9$ located at the outer shell of core−shell NPs with no contribution of Au (the ε_r' of metallic Au is much higher in value). By increasing the number of donor chromophores per C$_{60}$> cage to four, the magnitude of the dielectric amplification effect was maximized. We hypothesized that the long-period accumulation (or trapping)[3−5] of photogenerated SPR energy in the intermediate gold layer sandwiched between the layers of C$_{60}$(>DPAF-C$_9$)$_x$-derived fullerosome membrane and highly magnetic core γ-FeO$_x$ NPs was effectively released at the light-off stage in a near-field to induce activation of the intra-molecular polarization of C$_{60}$-DPAF molecules. The polarization formed a positively charged electron-donor moiety of DPAF-C$_9$ and a negatively charged electron-acceptor moiety of the C$_{60}$> cage. These charged transient states were regarded as the origin of observed high permittivity-photoswitching capability of 4-D$_x$.

Furthermore, by considering the facts that only a small thin coating area of active RF-responsive materials and a relatively low fluence level were applied in the measurements of this study, detected magnitude of reflection changes (or RF-signal alternations) can be regarded as significant. Therefore, these results implied the feasibility in terms of tunability and modulation ability of SAR-signals by 4-D$_1$ in either increase or decrease of its reflectivity to alter the image profile by variation of irradiation fluence. Good recyclability of ε_r' and ε_r'' back to their original values during each photoactivation cycle of light-on and light-off manipulations may allow the potential material uses as permittivity-photoswitching agents in RF-frequency devices by further enhancing the photoswitching effect.

■ ASSOCIATED CONTENT

Ⓢ Supporting Information

The Supporting Information is available free of charge on the ACS Publications website at DOI: 10.1021/acs.jpcc.6b05279.

> Synthetic procedures of 1-C$_9$, 2-C$_9$, and 3-C$_9$; MALDI-MS spectroscopic spectra of 1-C$_9$ and 2-C$_9$; preparation methods of core−shell nanoparticles 4-D$_x$; nanosecond transient charge-separated state spectra of 1-C$_9$ and 3-C$_9$; photophysical energy diagram of 3-C$_9$; frequency-dependent relative dielectric constant and loss factor data; dielectric measurement diagram; permittivity and SAR measurement setup diagrams (PDF)

■ AUTHOR INFORMATION

Corresponding Author
*Tel.: 978-934-3663. Fax: 978-934-3013. E-mail: Long_Chiang@uml.edu.

Author Contributions
All authors contributed equally to this work.

Notes
The authors declare no competing financial interest.

■ REFERENCES

(1) For a review: Ghosh, S. K.; Pal, T. Interparticle Coupling Effect on the Surface Plasmon Resonance of Gold Nanoparticles: from Theory to Applications. *Chem. Rev.* **2007**, *107*, 4797−4862.

(2) For an overview: Coronado, E. A.; Encina, E. R.; Stefani, F. D. Optical Properties of Metallic Nanoparticles: Manipulating Light, Heat, and Forces at the Nanoscale. *Nanoscale* **2011**, *3*, 4042−4059.

(3) Kelly, K. L.; Coronado, E.; Zhao, L. L.; Schatz, G. C. The Optical Properties of Metal Nanoparticles: the Influence of Size, Shape, and Dielectric Environment. *J. Phys. Chem. B* **2003**, *107*, 668−677.

(4) Novotny, L.; Hecht, B. *Principle of Nano-Optics*; Cambridge University Press: New York, 2006; and references therein.

(5) Mertz, J. Radiative Absorption, Fluorescence, and Scattering of a Classical Dipole Near a Lossless Interface: a Unified Description. *J. Opt. Soc. Am. B* **2000**, *17*, 1906−1913.

(6) Luk'yanchuk, B.; Zheludev, N. I.; Maier, S. A.; Halas, N. J.; Nordlander, P.; Giessen, H.; Chong, C. T. The Fano Resonance in Plasmonic Nanostructures and Metmaterials. *Nat. Mater.* **2010**, *9*, 707−715.

(7) Stuart, H. R.; Hall, D. G. Island Size Effects in Nanoparticle-Enhanced Photodetectors. *Appl. Phys. Lett.* **1998**, *73*, 3815.

(8) Atwater, H. A.; Polman, A. Plasmonics for Improved Photovoltaic Devices. *Nat. Mater.* **2010**, *9*, 205−213.

(9) Pillai, S.; Green, M. A. Plasmonics for Photovoltaic Applications. *Sol. Energy Mater. Sol. Cells* **2010**, *94*, 1481−1486.

(10) Losurdo, M.; Giangregorio, M. M.; Bianco, G. V.; Sacchetti, A.; Capezzuto, P.; Bruno, G. Enhanced Absorption in Au Nanoparticles/a-Si:H/c-Si Heterojunction Solar Cells Exploiting Au Surface Plasmon Resonance. *Sol. Energy Mater. Sol. Cells* **2009**, *93*, 1749−1754.

(11) Wang, M.; Su, C.; Yu, T.; Tan, L.-S.; Hu, B.; Urbas, A.; Chiang, L. Y. Novel Photoswitchable Dielectric Properties on Nanomaterials of Electronic Core-Shell γ-FeO$_x$@Au@fullerosomes for GHz Frequency Applications. *Nanoscale* **2016**, *8*, 6589−6599.

(12) Wang, M.; Jeon, S.; Su, C.; Yu, T.; Tan, L.-S.; Chiang, L. Y. Synthesis of Photoswitchable Magnetic Au−Fullerosome Hybrid Nanomaterials for Permittivity Enhancement Applications. *Molecules* **2015**, *20*, 14746−14760.

(13) Padmawar, P. A.; Rogers, J. O.; He, G. S.; Chiang, L. Y.; Canteenwala, T.; Tan, L.-S.; Zheng, Q.; Lu, C.; Slagle, J. E.; Danilov, E.; et al. Large Cross-Section Enhancement and Intramolecular Energy Transfer upon Multiphoton Absorption of Hindered Diphenylamino-fluorene-C$_{60}$ Dyads and Triads. *Chem. Mater.* **2006**, *18*, 4065−4074.

(14) Elim, H. I.; Anandakathir, R.; Jakubiak, R.; Chiang, L. Y.; Ji, W.; Tan, L. S. Large Concentration-Dependent Nonlinear Optical Responses of Starburst Diphenylaminofluorenocarbonyl Methano[60]fullerene Pentaads. *J. Mater. Chem.* **2007**, *17*, 1826−1838.

(15) Soumekh, M. *Synthetic Aperture Radar Signal Processing with MATLAB Algorithms*; John Wiley & Sons: New York, 1999.

(16) Kong, J. A. *Electromagnetic Wave Theory*; EMW Publication: Cambridge, MA, 2000.

(17) Ishimaru, A. *Electromagnetic Wave Propagation, Radiation, and Scattering*; Prentice Hall: Upper Saddle River, NJ, 1991.

(18) Chiang, L. Y.; Padmawar, P. A.; Canteenwala, T.; Tan, L. S.; He, G. S.; Kannan, R.; Vaia, R.; Lin, T. C.; Zheng, Q.; Prasad, P. N. Synthesis of C_{60}-Diphenylaminofluorene Dyad with Large 2PA Cross-Sections and Efficient Intramolecular Two-Photon Energy Transfer. *Chem. Commun.* **2002**, 1854.

(19) Luo, H.; Fujitsuka, M.; Araki, Y.; Ito, O.; Padmawar, P.; Chiang, L. Y. Inter- and Intramolecular Photoinduced Electron-Transfer Processes Between C_{60} and Diphenylaminofluorene in Solutions. *J. Phys. Chem. B* **2003**, *107*, 9312−9318.

(20) El-Khouly, M. E.; Anandakathir, R.; Ito, O.; Chiang, L. Y. Prolonged Charge-Separated States of Starburst Tetra-(diphenylaminofluoreno)[60]fullerene Adducts upon Photoexcitation. *J. Phys. Chem. A* **2007**, *111*, 6938−6944.

(21) Anandakathir, R.; Tan, L.-S.; Chiang, L. Y. Starburst Encapsulation of C_{60} by Multiple Hindered Two-Photon Absorptive Diphenylaminodialkylfluorene Arms. *J. Macromol. Sci., Part A: Pure Appl.Chem.* **2007**, *44*, 1265−1273.

(22) Padmawar, P. A.; Canteenwala, T.; Tan, L.-S.; Chiang, L. Y. Synthesis and Characaterization of Two-Photon Absorbing Diphenylaminofluorenocarbonyl-methano[60]fullerenes. *J. Mater. Chem.* **2006**, *16*, 1366−1378.

(23) Park, J.; An, K.; Hwang, Y.; Park, J. G.; Noh, H. J.; Kim, J. Y.; Park, J. H.; Hwang, N. M.; Hyeon, T. Ultra-Large-Scale Synthesis of Monodisperse Nanocrystals. *Nat. Mater.* **2004**, *3*, 891−895.

(24) Ohno, T. R.; Chen, Y.; Harvey, S. E.; Kroll, G. H.; Weaver, J. H.; Haufler, R. E.; Smalley, R. E. C_{60} Bonding and Energy-Level Alignment on Metal and Semiconductor Surfaces. *Phys. Rev. B: Condens. Matter Mater. Phys.* **1991**, *44*, 13747−13755.

(25) Kuzume, A.; Herrero, E.; Feliu, J. M.; Nichols, R. J.; Schiffrin, D. J. Fullerene Monolayers Adsorbed on High Index Gold Single Crystal Surfaces. *Phys. Chem. Chem. Phys.* **2004**, *6*, 619−625.

(26) Yong, V.; Hahn, H. T. Synergistic Effect of Fullerene-Capped Gold Nanoparticles on Graphene Electrochemical Supercapacitors. *Adv. Nanopart.* **2013**, *2*, 1−5.

(27) Islam, M. T.; Molugu, S. K.; Cooke, P. H.; Noveron, J. C. Fullerene Stabilized Gold Nanoparticles. *New J. Chem.* **2015**, *39*, 5923−5923.

(28) Bubnis, G. J.; Cleary, S. M.; Mayne, H. R. Self-Assembly and Structural Behavior of a Model Rigid C_{60}-Terminated Thiolate on Au(111). *Chem. Phys. Lett.* **2009**, *470*, 289−294.

(29) Shirai, Y.; Cheng, L.; Chen, B.; Tour, J. M. Characterization of Self-Assembled Monolayers of Fullerene Derivatives on Gold Surfaces: Implications for Device Evaluations. *J. Am. Chem. Soc.* **2006**, *128*, 13479−13489.

(30) Verma, S.; Hauck, T.; El-Khouly, M. E.; Padmawar, P. A.; Canteenwala, T.; Pritzker, K.; Ito, O.; Chiang, L. Y. Self-Assembled Photoresponsive Amphiphilic Diphenylaminofluorene-C_{60} Conjugate Vesicles in Aqueous Solution. *Langmuir* **2005**, *21*, 3267−3272.

(31) Hunt, M. R. C.; Modesti, S.; Rudolf, P.; Palmer, R. E. Charge Transfer and Structure in C_{60} Adsorption on Metal Surface. *Phys. Rev. B: Condens. Matter Mater. Phys.* **1995**, *51*, 10039−10047.

(32) Bensasson, R. V.; Garaud, J.-L.; Leach, S.; Miquel, G.; Seta, P. Transmembrane Electron Transport Mediated by Photoexcited Fullerene. *Chem. Phys. Lett.* **1993**, *210*, 141−148.

(33) Cushing, S. K.; Li, J.; Meng, F.; Senty, T. R.; Suri, S.; Zhi, M.; Li, M.; Bristow, A. D.; Wu, N. Photocatalytic Activity Enhanced by Plasmonic Resonant Energy Transfer from Metal to Semiconductor. *J. Am. Chem. Soc.* **2012**, *134*, 15033−15041.